PERGAMON

Journal of Structural Geology 24 (2002) 1789–1803

JOURNAL OF STRUCTURAL GEOLOGY

www.elsevier.com/locate/jstrugeo

# Numerical modelling of asymmetric boudinage

C.W. Passchier[a,*], E. Druguet[b]

[a]Institut fur Geowissenschaften, Johannes Gutenberg Universitat, Becherweg 21, D-55099 Mainz, Germany
[b]Departament de Geologia, Universitat Autònoma de Barcelona. 08193 Bellaterra, Barcelona, Spain

Received 20 April 2001; revised 7 November 2001; accepted 9 November 2001

**Abstract**

Asymmetric boudinage structures are commonly used as shear sense indicators but their development is incompletely understood. This paper describes the influence of initial shape and kinematic parameters on the evolution of boudin trains using a numerical approach based on the finite difference code FLAC. Boudin trains are simulated as a series of competent objects embedded in a soft matrix subjected to general monoclinic ductile flow.

Deformation of boudin trains includes heterogeneous stretching, rotation of boudins and offset along the neck regions. The sense of relative boudin offset is mainly influenced by the initial orientation of the interboudin plane in the boudinaging layer, while kinematic vorticity number of the flow and the orientation of the boudin train with respect to the flow extensional eigenvector, usually the shear zone boundary, also play a role. Viscosity ratio and aspect ratio influence the magnitude of offset along the neck regions and the amount of rotation of boudins but not the sense of slip and rotation on the interboudin plane. Knowledge of the orientation of the interboudin plane itself is insufficient to use asymmetric boudins as independent shear sense indicators. Details of the boudin geometry such as the sense of deflection of marker horizons along the interboudin plane must be used for this purpose. 

*Keywords*: Numerical modelling; Asymmetric boudins; FLAC

## 1. Introduction

Boudinage structures, first described by Ramsay (1881) and Lohest (1909), are a common and conspicuous feature in deformed rocks. Boudins occur as a subdivision of a planar volume of rock by regularly spaced veins or zones of enhanced deformation, the interboudin zones or boudin necks. This planar rock volume can be a layer, group of parallel layers or simply a domain of foliated rock (Fig. 1). In three dimensions, most boudins occur as long tabular strips separated by boudin necks. However, if deformation deviates from plane strain, more complex shapes such as chocolate tablet boudinage, with rectangular or cushion-shaped boudins, may develop.

In cross-section normal to the boudinaged planar volume of rock and the boudin necks, individual boudins occur in a range of shapes. Many boudins are rectangular or lens-shaped and arranged in a linear train of orthorhombic symmetry but there are also some, especially in ductile shear zones, with parallelogram-shaped cross-sections and/or relative displacement on the interboudin zone (Figs. 1 and 2a); such boudins have a monoclinic- or triclinic symmetry and are popularly known as *asymmetric boudins*. Their geometry suggests that they carry information on the rotational component of progressive deformation, and could act as shear sense indicators (Hanmer, 1986; Gaudemer and Taponnier, 1987; Malavieille, 1987; Marcoux et al., 1987; Goldstein, 1988; Malavieille and Lacassin, 1988; Hanmer and Passchier, 1991). Asymmetric boudins are potentially useful in medium to high-grade metamorphic terrains where shear sense markers are generally rare.

In monoclinic non-coaxial flow in which the vorticity vector parallels a boudinaging layer, two main kinematic types of asymmetric boudins can be envisaged, distinguished by the sense of offset or slip on the interboudin zone compared with bulk shear sense: *synthetic slip* or *antithetic slip* boudins (Hanmer, 1986; Fig. 2a). Both types occur in nature but, as shown in Fig. 2b, it is not straightforward how synthetic and antithetic slip boudins in Figs. 1 or 2a should be distinguished if shear sense is unknown. Synthetic and antithetic slip boudins can therefore only be used as independent shear sense indicators if characteristic differences in geometry are identified. Synthetic slip boudins commonly show a small angle

* Corresponding author. Tel.: +49-6131-393217; fax: +49-6131-393863.

*E-mail addresses:* jsg@mail.uni-mainz.de (C.W. Passchier), cpasschi@mail.uni-mainz.de (C.W. Passchier), elena.druguet@uab.es (E. Druguet).

0191-8141/02/$ - see front matter 
PII: S0191-8141(01)00163-8

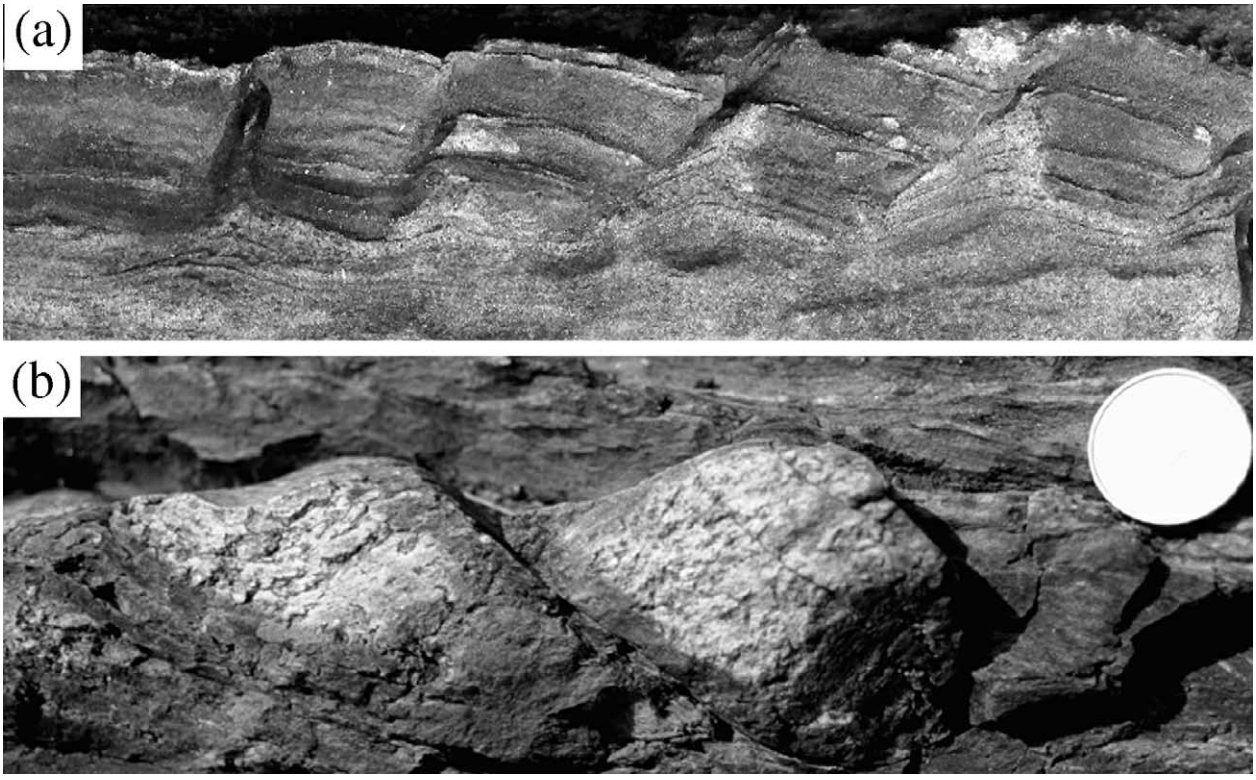


Fig. 1. Natural examples of asymmetric boudins. (a) Boudinaged quartz-rich layer in carbonate with antithetic slip with respect to shear sense. Kaoko belt, Namibia. Width of the photograph: 30 cm. (b) Boudinaged amphibolite layer with synthetic slip in pelitic–psammitic schists. Cap de Creus peninsula, NE Spain. Width of view: 18 cm. Sense of shear is dextral in both cases.

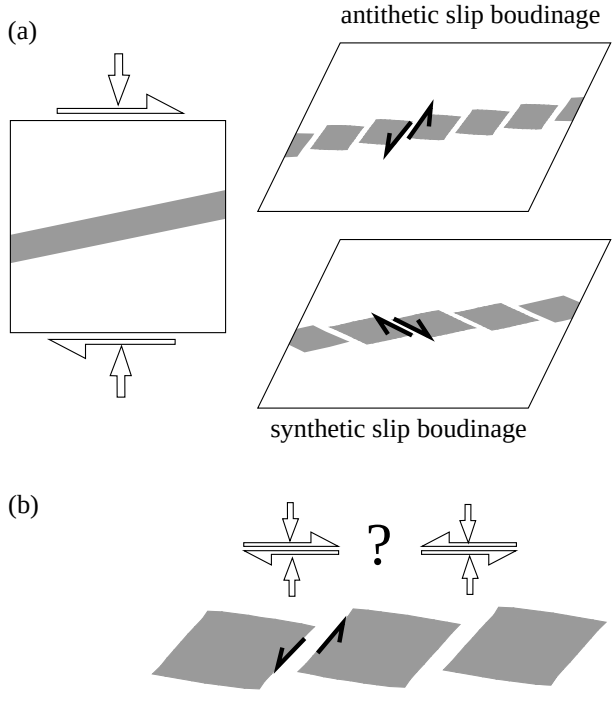


Fig. 2. (a) Schematic presentation of the main kinematic types of asymmetric boudinage based on sense of offset along the interboudin plane and orientation of this plane. (b) Possible asymmetric boudin geometry—from this geometry alone, it is not possible to determine which of the cases in (a) applies.

between the interboudin zone and the exterior boudin surface (Cloos, 1947; Goldstein, 1988; Jordan, 1991; Swanson, 1992) while antithetic slip boudins are of a more rectangular shape (Etchecopar, 1977; Hanmer, 1986; Malavieille and Lacassin, 1988; Swanson, 1992). Further progress in the understanding of asymmetric boudins can be gained either through detailed studies of natural boudins under simple well-documented deformation conditions, e.g. where deformation kinematics are known to some extent, or from physical or numerical models for flow types more complex than simple shear. Field observations are suitable to determine which geometric types are common in nature, which geometric elements occur in each boudin type and to investigate relationships between boudin geometry and the sense of interboudin slip (synthetic and antithetic). This has been attempted by, among others, Hanmer (1986), Goldstein (1988), Swanson (1992) and Goscombe and Passchier (2002). Numerical and analogue experiments, however, allow a more precise analysis of the influence of a large number of variables on boudin shape and arrangement.

Physical analogue modelling of asymmetric boudinage was carried out by Ramberg (1955), Ramsay (1967), Ghosh and Ramberg (1976) and more recently by Hanmer (1986), Goldstein (1988), Mandal and Khan (1991) and Mandal et al. (2000). Previous attempts to numerically model boudinage mostly dealt with the mechanisms of

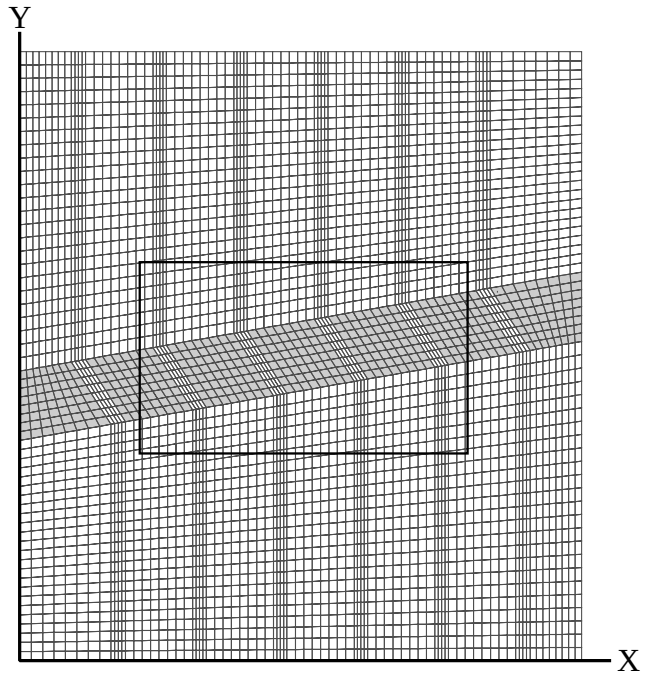


Fig. 3. Example of a finite difference grid used in the numerical simulation. Grey elements are more viscous than white ones. The rectangle delimits the area from which data on deformed boudins have been analysed.

fracture and necking during layer-normal compression. Stress distribution and boudin displacement have been investigated with the use of the finite element method (FEM) and through theoretical considerations of elastic rock behaviour (Stephanson and Berner, 1971; Strömgard, 1973; Selkman, 1978; Treagus and Lan, 2000). Lloyd and Ferguson (1981) used FEM to analyse stress distribution, separation and shape variation during post-fracture ductile deformation, boudin rheology being modelled in that case as an elastic–plastic material.

In this study we analyse asymmetric boudinage using the commercial code FLAC (Itasca Consulting Group, Inc., 1998) to perform numerical simulations on the rotation and deformation of pre-fractured boudins. One of the problems for experimental work is the large number of parameters that can play a role in the development of asymmetric boudins. Even in two dimensions these include several factors describing initial boudin shape and orientation, factors describing boudin and matrix rheology and factors describing the bulk flow. Most of these factors are independent, which means that a very large number of experiments are needed to test the effects of all of these. For practical purposes, we decided to attempt modelling the development of asymmetric boudins numerically using a minimum number of geometric, kinematic and rheological parameters in a two-dimensional (2D) homogeneous monoclinic flow. Even if this is insufficient to fully model the whole range of natural boudin shapes, it serves as an indication of the parameters that are most important in determining the final shape and arrangement of asymmetric boudins. Our main objective is to see how the synthetic and antithetic nature of interboudin slip is established and how this depends on boudin shape and flow parameters.

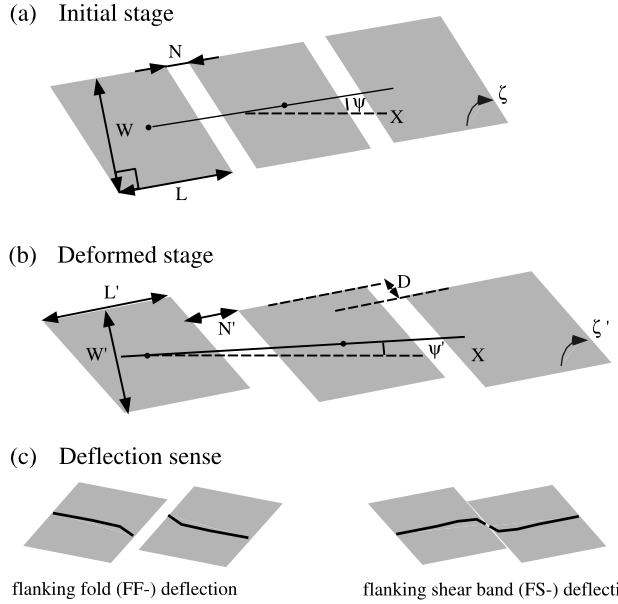


Fig. 4. Geometrical parameters involved in numerical simulation. (a) Initial stage. $L$—boudin length, $W$—boudin width, $N$—neck width or boudin separation. (b) Deformed stage. $L'$—length of deformed boudin, $W'$—width of deformed boudin, $N'$—width of deformed neck measured parallel to $L'$, $D$-displacement along the interboudin plane. (c) Two opposite geometries of deflection sense of an internal marker in boudins.

## 2. Method

FLAC is a 2D explicit finite difference code whereby the differential equations are solved alternately, with the output for the solution of the equations of motion used as input to the constitutive equations for a progressive calculation. FLAC is based on 4-node quadrilateral meshes formed by superposing two constant stress/constant strain triangular finite elements. Each element behaves according to a prescribed linear or non-linear stress/strain law in response to the applied forces or velocity boundary conditions. It offers a rather wide range of capabilities to solve complex problems in geology. It has been used for studies of localisation of shear bands and fractures (Hobbs and Ord, 1989; Ord, 1990; Cundall, 1991; Poliakov and Herrmann, 1994; McKinnon and Garrido de la Barra, 1998; Gutierrez and Cuisiat, 1999), buckling and fold development (Zhang et al., 1996), diapirism (Poliakov et al., 1996), ice flow (Wilson and Zhang, 1994; Marmo and Wilson, 1999) and fabric development in polycrystalline aggregates (Zhang et al., 1994).

Since it is difficult to have interfaces fill and expand with progressive deformation, our models are based on already existing boudins with a slight separation. We therefore only consider the post-initiation ductile component of boudin

Table 1
Value of parameters used in the base model

| | | | |
|---|---|---|---|
| Boudins shape | Shape factor | $L_R$ | 1 |
| | Separation factor | $N_R$ | 0.2 |
| Elastic properties | Matrix bulk modulus | $K_m$ | 2.0e10 Pa |
| | Matrix shear modulus | $G_m$ | 1.2e10 Pa |
| | Boudin bulk modulus | $K_b$ | 4.0e10 Pa |
| | Boudin shear modulus | $G_b$ | 2.4e10 Pa |
| | Poisson's ratio for matrix and boudins | $\nu$ | 0.25 |
| Viscous properties | Matrix viscosity | $\eta_m$ | 1.0e19 Pa s |
| | Boudin viscosity | $\eta_b$ | 1.0e20 Pa s |
| | Viscosity constrast | $M$ | 10 |
| Bulk stretching rate | | | 1.0e − 14 $s^{-1}$ |

development. This is not completely satisfactory, since boudin initiation is a complex function of many parameters such as rheology of matrix and boudinaging layers, the nature of older fabric elements and fluid pressure and composition. However, our method is a first approximation to investigate the influence of a large number of parameters on the shape of asymmetric boudins once interboudin zones have initiated.

Boudin trains are simulated in the FLAC grid as a series of quadrilateral objects embedded in a softer matrix (Fig. 3). The interboudin zones are given the same rheology as the matrix, or a rheology different from boudins and matrix. For most experiments we used a grid of $80 \times 56$ elements, with a central train of five quadrilateral objects and two objects at the outer edge with shapes adapted to the left and right boundaries of the model (Fig. 3). Each quadrilateral 'boudin' consist of $8 \times 8$ elements and the interboudin zones are four elements wide (Fig. 3). We found that this grid density gave optimal results at minimal calculation time, as discussed in Section 5.3.

We use an algorithm that allows the grid to be variably distorted to obtain different initial shapes and orientations of the boudin train to be modelled. The initial geometry of the boudin train is defined by the following parameters (Fig. 4a):

1. A shape factor $L_R = L/W$, the ratio of the initial boudin length ($L$) to boudin width ($W$).
2. A separation factor $N_R = N/L$, the neck width ($N$) to boudin length ($L$) ratio.
3. An angle $\psi$, the orientation of the boudin train with respect to the base of the grid which is parallel to the $X$-axis of a Cartesian coordinate system. The base of the grid is allowed to stretch but not to rotate during progressive deformation and is therefore parallel to the extensional bulk flow eigenvector (Fig. 4). $\psi$ has a positive sign if measured anticlockwise and negative if measured clockwise from the $X$-axis.
4. An angle $\zeta$, the orientation of the plane parallel to the interboudin zone (interboudin plane) with respect to the boudin outer surface, measured clockwise (rectangular boudins if $\zeta = 90°$; Fig. 4).

## 3. Material properties and boundary conditions

For most numerical simulations we adopted a linear elasto-viscous (Maxwell) material model (Turcotte and Schubert, 1982). This rheology is equivalent to a combination in series of an elastic element and a Newtonian viscous element. According to this constitutive model, the rate of strain is the superposition of a linear elastic strain rate and a linear viscous strain rate. Therefore the total strain rate satisfies

$$\frac{d\epsilon}{dt} = \frac{\sigma}{2\mu} + \frac{d\sigma}{E dt} \quad (1)$$

where $E$ is the Young's modulus and $\mu$ the viscosity. The material behaves like an elastic material for loads of short duration but like a Newtonian viscous material over a long period, so that permanent strain accumulates viscously, starting as soon as stress is applied. Elasto-viscous behaviour is useful in modelling the response of crustal rocks at high temperature and high confining pressure.

As an approximation to the rheology of real rocks, material constants within the range of experimentally derived rheologies (Turcotte and Schubert, 1982) have been assigned to the models. These constants are also within the range of those employed by Zhang et al. (1996) and Mancktelow (1999) in their numerical models of single-layer folding. The rheology of the modelled boudins differs from that of the matrix in both elastic and viscous constants, the boudins having higher bulk and shear elastic moduli and viscosity. Poisson's ratio is 0.25 for both layer and matrix. The rheological response according to the values used (listed in Table 1) is close to purely viscous. The algorithm that we used allows the grid to deform by area-constant monoclinic flow (Jiang and Williams, 1998; Passchier, 1998) with a dextral vorticity component. The (extensional) eigenvector lies parallel to the $X$-axis of the grid with the origin in the left-lower corner of the grid. Velocity boundary conditions were applied on grid points on the four sides of the model such that the outer boundaries remain straight and parallel forming a parallelogram. This implies that each grid point along the edge of the model moves at constant velocity during each experimental run, irrespective of flow conditions inside the model. These boundary velocities are calculated from general flow tensors and are expressed as a function of a bulk stretching rate and the 2D kinematic vorticity number ($W_k$) (Means et al., 1980; Passchier, 1998). The grid could thus deform within the whole range between pure shear and simple shear, corresponding to 2D transpression, by changing $W_k$ in the velocity functions. A constant stretching rate of 1e − 14 $s^{-1}$ was applied to the models. The maximum creep time increment (i.e. the ratio of the viscosity to the shear modulus for linear viscous flow) was set to 8e8 s in order to ensure mechanical equilibrium and numerical stability. With these values most models involved have on the order of 40000–50000 steps to attain a bulk strain axial ratio $R = 2$.

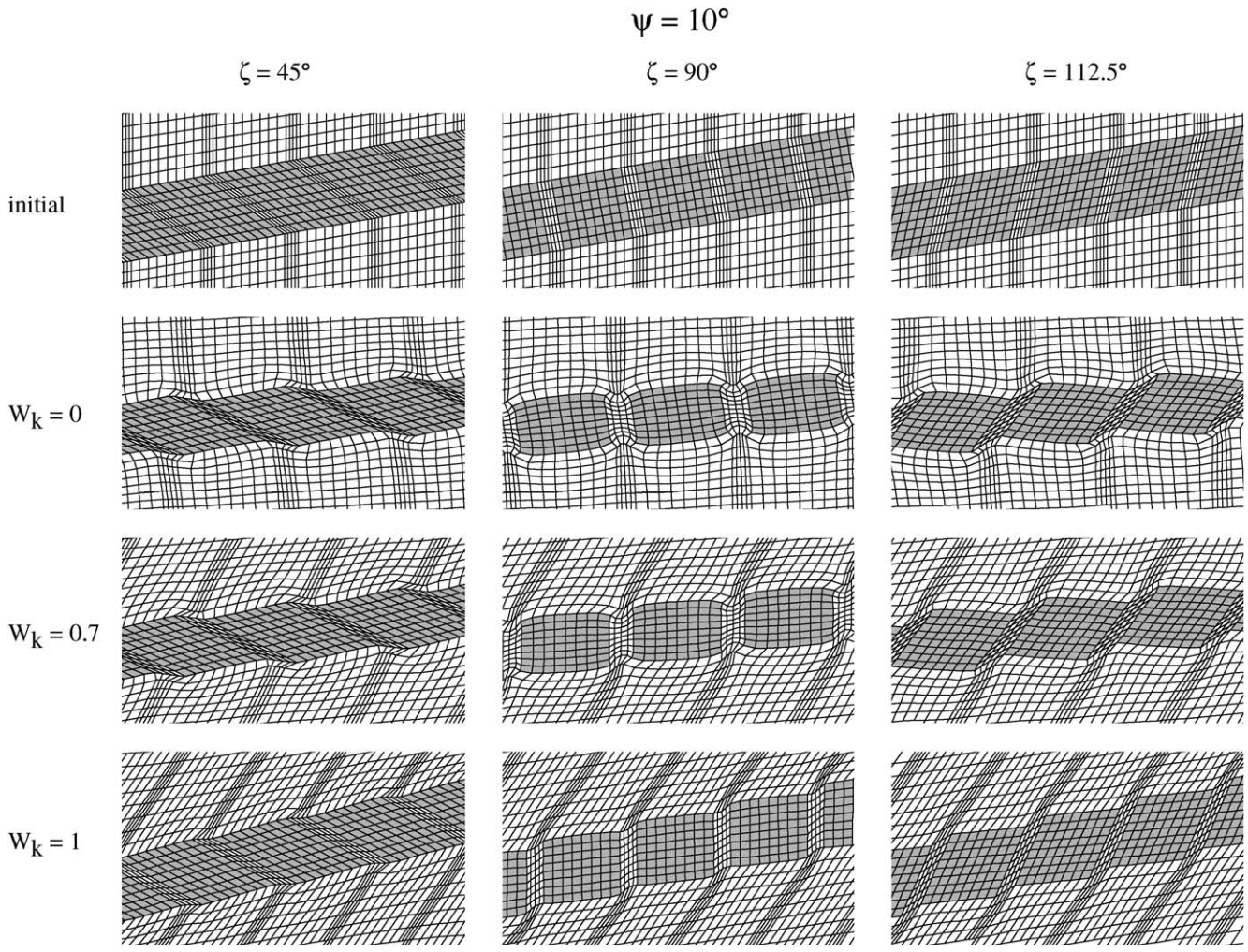


Fig. 5. Examples of central parts of base model grids for $\psi = 10°$ and variable $\zeta$ and $W_k$, deformed to a bulk strain ratio $R = 2$. The initial stages are shown in the first row.

The central grid segments that represent boudins were free to deform under the applied boundary conditions in bulk homogeneous flow, while segments in contact with the left and right margins of the model were fixed to the outer boundaries of the grid and therefore distorted by boundary effects (Fig. 3). This does not visibly affect the other boudins closer to the centre, but because of these boundary effects all measurements of changes in boudin shape were restricted to the three central boudins (area shown in Fig. 3). We also investigated the boundary effects by leaving the two 'edge-boudins' out, i.e. testing a short boudin train of five central boudins separated from the boundaries by matrix material. The results were slightly different in relative rates of displacement and rotation since the short train as a whole behaves as a more competent composite 'object' in a soft matrix and the matrix material tends to flow around the entire boudin train. We found that the first model, with boudins truncated by the side walls is a better approximation of a 'infinitely' long train of boudins in a layer. We have used this model throughout the experiments.

## 4. The base model

We first investigated the influence of the initial orientation of a boudinaged layer ($\psi$), the interboudin plane ($\zeta$) and flow kinematic vorticity number ($W_k$) upon the kinematic type of asymmetric boudins (synthetic or antithetic interboudin slip; Fig. 2) that develop. This is done for a fixed initial aspect ratio, separation and rheology of boudins and matrix as listed in Table 1. Five different values were investigated for each of the independent variables in order to cover the largest experimentally possible range of boudin geometry and flow kinematics:

1. $\psi$: −20, −10, 0, 10 and 20° (and some measurements at 30 and 40°)
2. $\zeta$: 45, 67.5, 90, 112.5 and 135°
3. $W_k$: 0 (pure shear), 0.38, 0.7, 0.92 and 1 (dextral simple shear)

It is conceivable that some $\psi$ and $\zeta$-values are not realised in nature or may lead to impossible arrangements. If the

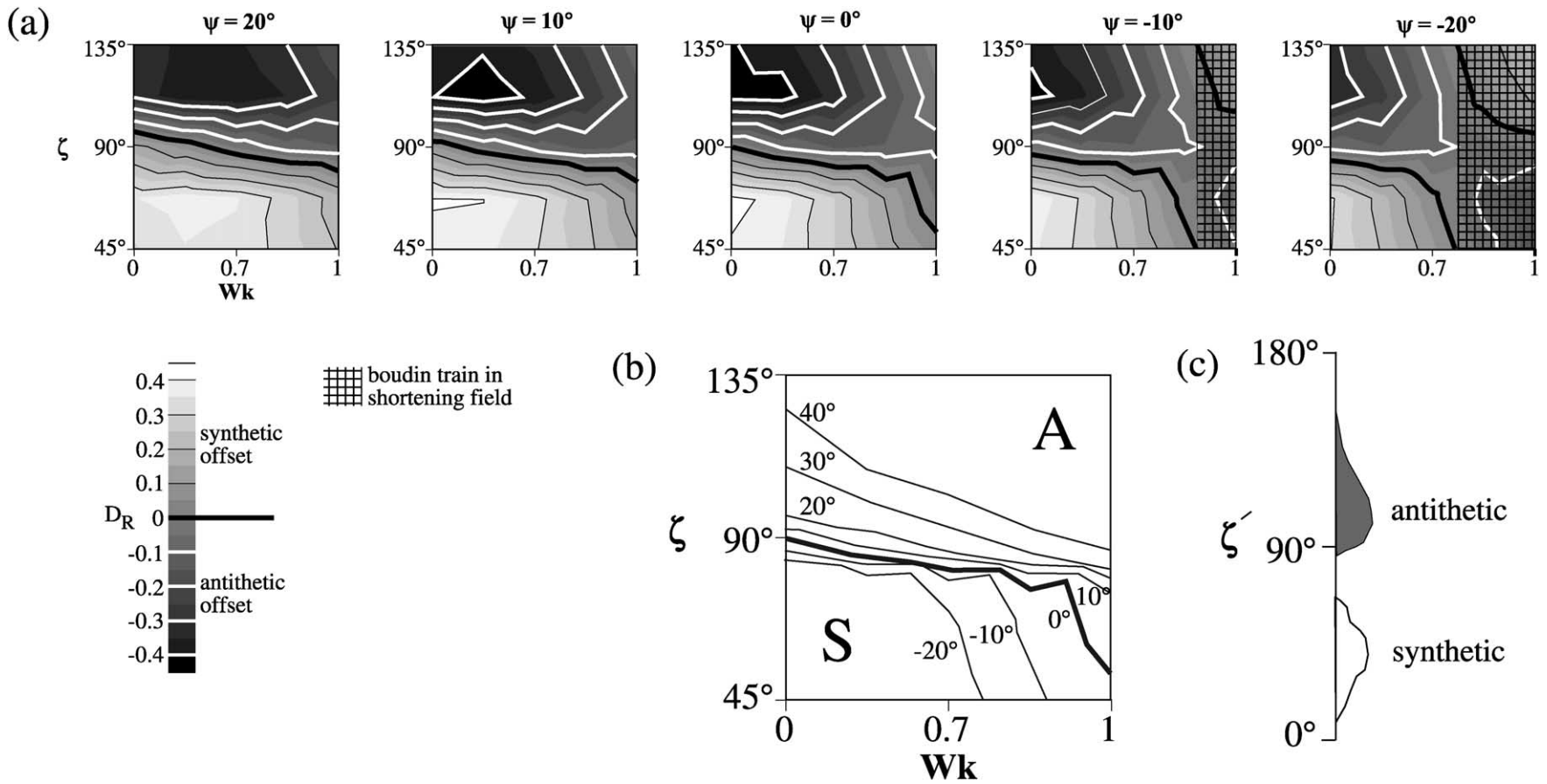


Fig. 6. (a) Contours of offset factor ($D_R$) plotted in diagrams of $W_k$ versus $\zeta$, for different $\psi$ values. All data derive from base model grids deformed to a bulk strain ratio $R = 2$ as shown in Fig. 5. (b) $D_R = 0$ curves for all investigated $\psi$ values separating antithetic ($A$) and synthetic ($S$) slip boudins at $R = 2$. (c) Distribution of natural boudins with antithetic and synthetic slip as a function of $\zeta'$ as observed by Goscombe and Passchier (2002).

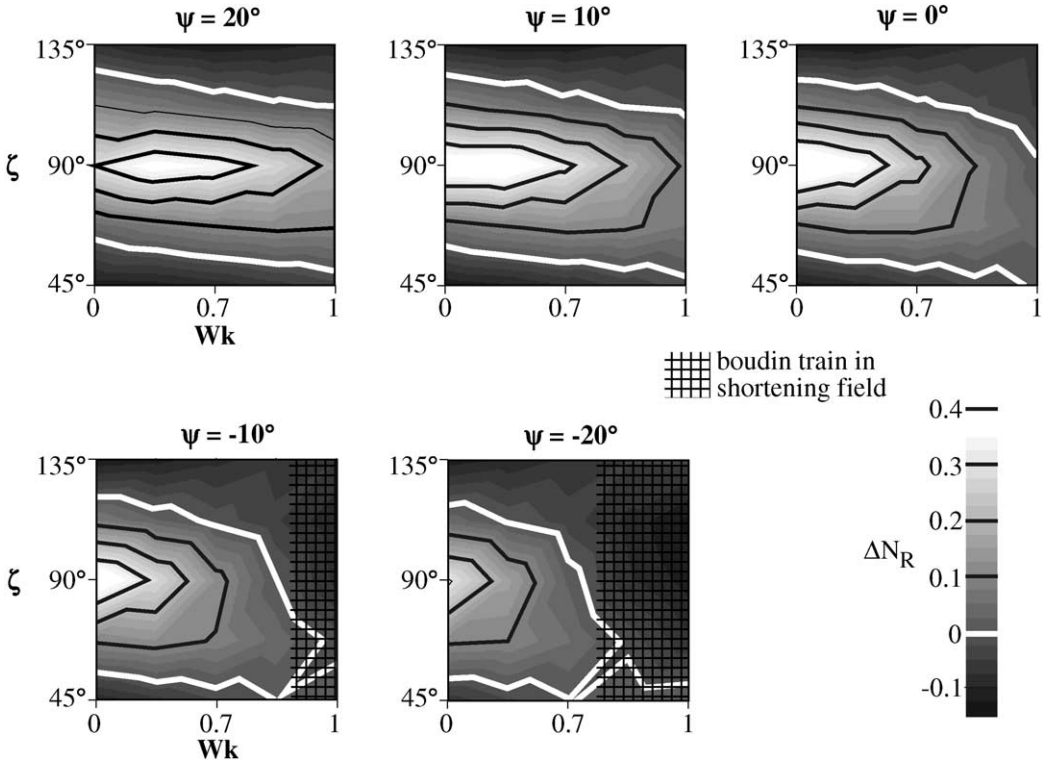


Fig. 7. Contours of boudin separation ($\Delta N_R$) plotted in diagrams of $W_k$ versus $\zeta$, for different $\psi$ values. All data derive from base model grids deformed to a bulk strain ratio $R = 2$. Solid white contour lines represent lines of no further separation.

initial boudin train is in the shortening field of flow, boudin separation does not occur and 'thrusting' can occur instead. This geometry is not considered in our model, and this explains the limitation of $\psi$ to low values in the experiments. The limits of realistic $\zeta$-values depend on the nature of initial boudinage. If boudinage is produced by brittle fracturing and the layer is loaded in extension, $\zeta$ is likely to lie between 50 and 130°, independent of the exact orientation of the layer with regard to the shear zone boundaries ($\psi$) and of the sense of flow in the host rock. This range of $\zeta$-values would embrace tensile fracture boudinage ($\zeta$-values around 90°), shear fracture boudinage and hybrid extensional shear fracture boudinage, as theoretically and experimentally modelled by Mandal and Khan (1991) and Mandal et al. (2000). If boudinage occurs by nucleation and growth of ductile shear bands in the boudinaging layer, then both the vorticity of the flow and the orientation of the layer in the kinematic frame play a role in the initial orientation of the interboudin zones. For $W_k = 1$ (simple shear) and at $\psi$-values close to zero, shear bands are likely to occur at $\zeta$-values between 30 and 60° where resolved shear stress is at a maximum in the shear band. For $W_k = 0$ (pure shear) and at $\psi$-values close to zero, conjugate sets could develop with one set at $30° < \zeta < 60°$ and the other at $120° < \zeta < 150°$ (see e.g. Kidan and Cosgrove, 1996). The situation becomes more uncertain for larger $\psi$-angles and $W_k$ values other than 0 and 1, mainly because there is as yet no unified theory of shear band formation in general monoclinic flow.

Due to limits imposed by the shape of the grid in our experiments, we could only model $\zeta$-values between 45 and 135°. This includes only part of the range of $\zeta$-values that may occur in nature, but we think that it is sufficient to show the general trends of asymmetric boudin development.

The possible combinations listed above result in a first series of 125 simulations grouped under the name 'base model'. Fig. 3 is an example of an undeformed base model with $\psi = 10°$ and $\zeta = 67.5°$. In each simulation, the grid was deformed until a bulk strain axial ratio of $R = 2$ was reached (Fig. 5). At several deformation stages, but particularly at the end of the simulations, flow patterns and the variation of different parameters were analysed as given below. Accented parameters are those measured in the deformed state. The most important ones are (Fig. 4b):

1. The length/width ratio of the deformed boudins expressed by the shape factor $L'_R = L'/W'$.
2. The ratio of slip or offset along the interboudin plane ($D$) against deformed boudin width, expressed as the offset factor $D_R = D/W'$.
3. The neck width to boudin length ratio of the deformed boudins expressed by the separation factor $N'_R = N'/L'$.
4. The ratio of the change in separation factor to the original

separation factor expressed as boudin separation $\Delta N_R = (N'_R - N_R)/N_R$.
5. The angle $\psi'$ of the median line of the deformed boudin train with respect to the $X$-axis (Fig. 4b).
6. $\zeta'$, the deformed equivalent of $\zeta$ measured in the boudins (Fig. 4b).
7. Strain distribution in the boudins (e.g. a barrelling effect).

Since we are mainly interested in the synthetic or antithetic nature of interboudin slip, we concentrate on the offset factor $D_R$ as a measure of type and degree of asymmetry (Fig. 4b). Synthetic and antithetic slip are indicated with positive and negative values of $D_R$, respectively.

## 5. Results for the base model

### 5.1. General results

The experiments with the base model illustrate how the initial geometries of boudins and boudin trains are modified by deformation. The nature and intensity of ductile deformation, relative rotation and offset of individual boudins depends strongly on initial geometric parameters and $W_k$ (Fig. 5). Antithetic or synthetic sense and amount of interboudin slip are determined by all three parameters $W_k$, $\psi$ and $\zeta$. The relative influence of each of these parameters on the development of asymmetric boudins can be expressed most easily in terms of the offset factor ($D_R$). In all models, $D_R$ increases logarithmically with strain. If $\psi = 10°$ (Fig. 5) antithetic slip prevails at $\zeta > 112.5°$ and synthetic at $\zeta < 45°$, regardless of $W_k$. However, at intermediate near-orthogonal $\zeta$ values, sense of slip depends on $\psi$ and $W_k$. The influence of $W_k$, $\psi$ and $\zeta$ is shown in Fig. 6a as contours of $D_R$. Each diagram is divided into domains of synthetic and antithetic slip, separated by a solid line where $D_R = 0$. The contours in each of the diagrams in Figs. 6a and 7 have been constructed from the results of 125 experiments.

In bulk flow with dextral shear sense, a boudin train rotates in the same sense as the imposed shear sense towards the extensional eigenvector if $\psi$ is positive, or if it is negative and

$$|\psi| > \arccos(W_k) \quad (2)$$

Where the initial boudin train is in the shortening field of flow, boudin separation does not occur and 'thrusting' occurs instead. These parts of the diagrams can therefore be ignored and are not further analysed (hatching in Figs. 6a and 7). In natural shear zones, the extensional eigenvector seems to be close to the shear zone boundary in most cases (Passchier, 1998). Observations on strain gradients and associated boudinage development during a single deformation event in natural shear zones suggest that most boudinage in dextral shear occurs for positive $\psi$-values (Hanmer and Passchier, 1991). For these $\psi$-values, the influence of $\zeta$ on $D_R$ is greater than that of $\psi$ and $W_k$ (Fig. 6a and b). The boundary of zero $D_R$ is located around $\zeta = 90°$ and intensities of synthetic and antithetic slip increase away from this value. However, for bulk flow approaching simple shear and $\psi$ close to zero, the $D_R$ curves start to bend sharply down close to $W_k = 1$ (simple shear). This implies that for low $\psi$-values, antithetic slip boudinage will prevail in simple shear dominated flows above $\zeta \approx 55°$. These observations are consistent with results obtained by O'Driscoll (1964), Hanmer (1986) and Goldstein (1988) using real model materials. Synthetic slip is clearly favoured in lower $W_k$ flow, a trend also suggested for the development of shear band cleavage which can be regarded as a special case of synthetic foliation boudinage (Hanmer, 1986; Goldstein, 1988; Swanson, 1992). Goscombe and Passchier (2002) investigated the shape of natural boudins formed at inferred low positive $\psi$ and simple shear or transpressional deformation conditions ($W_k < 1$) and found that antithetic and synthetic slip boudins show a distinct distribution of $\zeta'$ values as illustrated in Fig. 6c. This distribution shows an interesting similarity to our results.

Fig. 5 also gives information on the development of other geometrical elements such as 'barrelling' (deflection from a parallelogram shape to a rounded geometry) and boudin separation due to layer-parallel extension ($\Delta N_R$). These are primarily influenced by $\zeta$ and to a lesser extent by $\psi$ and $W_k$, the models reaching strongest barrelling and maximum separation for $\zeta = 90°$, $\psi = 0°$ and $W_k = 0$ (Figs. 5 and 7).

The circumstances under which barrelling occurs in our experiments are in agreement with results obtained by Treagus and Lan (2000) from FEM analysis of viscous objects subjected to bulk pure shear, where squares orthogonal to the strain axes show more tendency to deform into a barrel-shape than diagonal squares of the same viscosity contrast.

The increase in boudin separation with $\zeta$ approaching 90° (Fig. 7) is in agreement with observations on natural boudins made by Goscombe and Passchier (2002). They found that separation across interboudin zones almost never occurred in low $\zeta$ boudins but was present, with or without vein infill, in most symmetric boudins and asymmetric boudins with $\zeta$ values approaching 90°. Furthermore, our numerical results show that for low $\psi$ values, boudin separation decreases with increasing $W_k$. This means that the amount of boudin separation carries information on the vorticity of the operating bulk flow.

### 5.2. Flanking structures

An important effect of internal deformation of boudins is the deflection of marker planes in boudins in a narrow strip flanking the interboudin zone (Fig. 4c: Hudleston, 1989; Swanson, 1992; Druguet et al., 1997; Grasemann and Stüwe, 2001; Passchier, 2001). Deflection may be of a geometry as expected for drag on shear zones (flanking

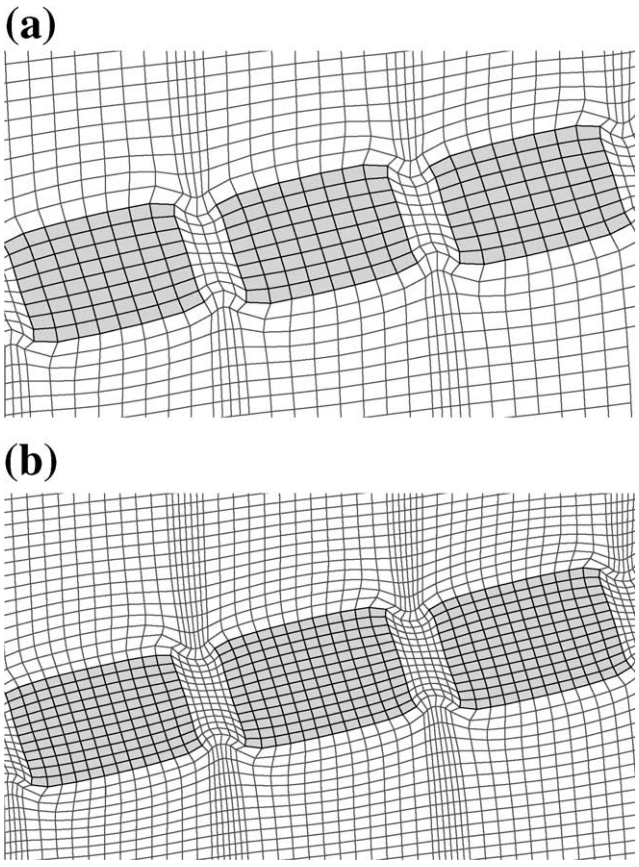


Fig. 8. Comparison of the effect of different mesh sizes upon a model with $\psi = 20°$, $\zeta = 90°$ and $W_k = 0$ after a strain ratio $R = 2$. (a) Standard mesh size used in this study. (b) Mesh resolution increased 1.5 ×.

shearband-deflection or FS-deflection), or of opposite sense (flanking fold deflection or FF-deflection). Because low to moderate strain was achieved in our experiments we only observed weak deflections (Fig. 5) but these show a clear trend. FS-deflection of gridlines mainly occurs at low or high $\zeta$-values (45 and 135°), since slip along interboudin zones is significant and boudin separation is low; it forms by a gradient of decreasing strain from the centre of the interboudin zone towards the boudins, like in shear bands. On the contrary, FF-deflection mainly occurs at $\zeta$-values closer to 90° and, very weakly, at $\psi = 0°$ and low $\zeta$-values (45°). This is attributed to a mechanism first postulated by Hudleston (1989) where slip takes place in the interboudin zone while it rotates passively in a flow field. In such cases, flow partitioning may cause a narrow strip along the interboudin zone to stretch coaxially and a fold structure characteristic of FF-deflection develops in marker planes (Fig. 4c; Passchier, 2001). FS- and FF-deflection may prove to be the most important criteria for distinguishing different types of asymmetric boudins.

### 5.3. Mesh resolution

In order to determine whether the finite difference mesh density that we used could be of influence on the final results, we ran a few simulations with mesh resolution increased 1.5 ×. The redefined grids are 120 × 84 elements, each quadrilateral 'boudin' consisting of 12 × 12 elements and the interboudin zones six elements wide. Fig. 8 shows changes resulting from a 1.5 × increase in mesh resolution upon a model with $\psi = 20°$, $\zeta = 90°$ and $W_k = 0$, deformed up to a strain ratio $R = 2$. No effect of the mesh density other than more detail in the shape of deformed boudins could be established. Since execution times of algorithms increase with increasing mesh resolution, we found that the standard grid density used for the base model was appropriate for the aims of this analysis, giving optimal results at minimum calculation time. Denser grids give better graphics but only slightly more accurate results.

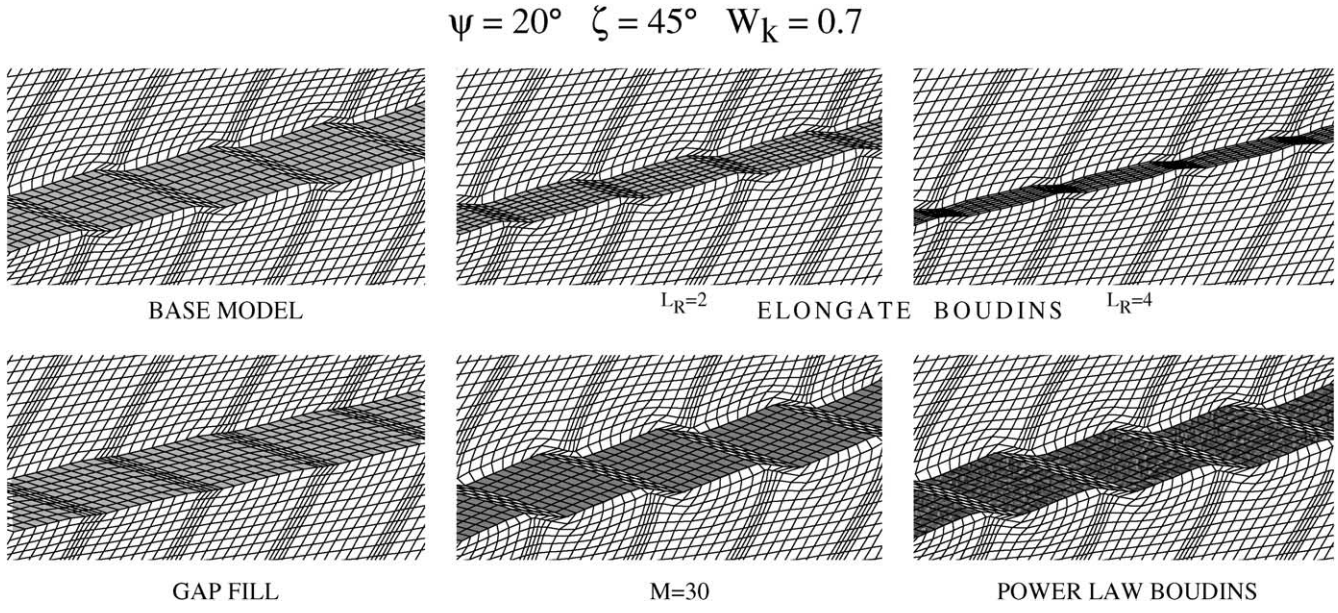


Fig. 9. Examples of central parts of models with different initial shape and rheology for $\psi = 20°$, $\zeta = 45°$ and $W_k = 0.7$, deformed to a bulk strain ratio $R = 2$.

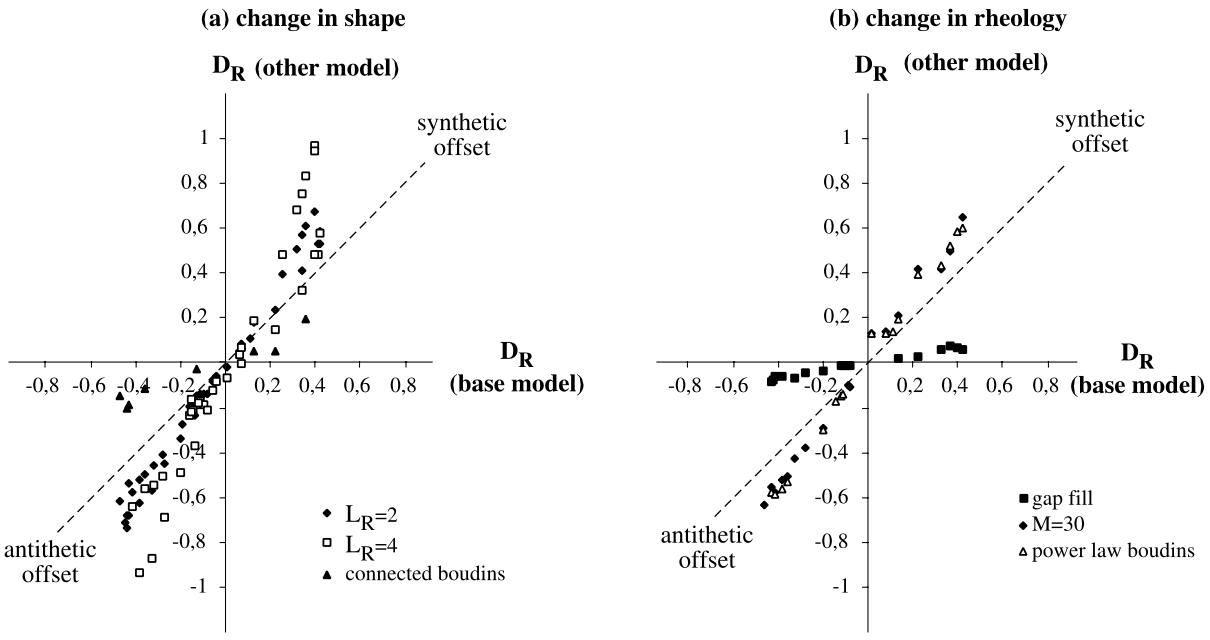


Fig. 10. Graphs of base model offset factor $D_R$ against $D_R$ in other models with different geometrical (a) and rheological (b) variables. All models are deformed to a bulk strain ratio $R = 2$. Dashed lines have a slope of one. Notice the increase in offset with increasing shape factor ($L_R$) and viscosity ratio, and decrease in offset in the models with filled gaps and connected boudins.

## 6. Other models—effects of shape and rheological factors

Asymmetric boudins are also influenced by other parameters than $\psi$, $\zeta$ and $W_k$. To test these effects we ran numerical experiments modifying either initial shape or rheological parameters from the base model. Not all the 125 base model runs were re-tested in each of these other models, but a selection of 15 to 45 end-member simulations. The following parameters were investigated.

*Elongate boudins*—these simulations use the same constant values as the base model (listed in Table 1) except for the length/width ratio $L_R$ of the boudins. Values of $L_R = 2$ and 4 were tested for different $\psi$, $\zeta$ and $W_k$. We found that boudin separation ($\Delta N_R$) increases with increasing boudin aspect ratio $L_R$. The amount of rotation of individual boudins for a particular bulk finite strain is slightly influenced by $L_R$ and the actual deviation depends on flow kinematics and the initial boudin geometry and orientation. However, the shape factor $L_R$ never affects the sense of rotation of individual boudins. $L_R$ has some influence on boudin shape, barrel-shaped irregularities being best developed in boudins with a more elongate initial shape (Fig. 9).

Fig. 10a shows the effect of a change in $L_R$ on $D_R$; the slopes of the mean trends in Fig. 10a are higher than one but the trend is not linear and the increase in $D_R$ with $L_R$ is larger for larger offsets. Fig. 11 shows three $D_R$ contour graphs for $\psi = 10°$, comparing models with $L_R = 1$, 2 and 4. Besides the overall increase in $D_R$ with aspect ratio, the shape of the contours differs significantly. However, despite the complicated relationship of actual $D_R$ values and $L_R$ the position of the $D_R = 0$ curve in Fig. 11 is hardly affected, i.e. there is *no* significant influence of $L_R$ on sense of slip along the interboudin planes. This means that the boundaries separating synthetic and antithetic fields in Fig. 6 are more or less identical for boudins of $L_R$ between 1 and 4.

*Connected boudins*—this model differs from the base model in that boudins with an aspect ratio $L_R = 2$ are connected centrally by necks half the width of the boudins. Both necks and boudins have the same viscosity ($\eta$= 1e20 Pa s). Connected boudins give lower boudin rotation, separation, and $D_R$ values, but no change in the sense of slip (Fig. 10a).

*Gap fill*—in this model, the material fill of the interboudin zones has a viscosity intermediate between that of the matrix and that of the boudins ($\eta$interboudin = 5 e19 Pa s). This is done to simulate interboudin gaps filled by other material than that of the matrix, such as due to precipitation from a fluid. An example of a deformed specimen is shown in Fig. 9. The boundaries of the boudinaged layer remain smooth after deformation since, with the filled necks, there is a lower contrast in rheology along the boudin train. Gap fill models therefore give much lower values of rotation, $L'_R$, and $D_R$ as the base model (Figs. 9 and 10b), but no change in the sense of slip. Comparison of $D_R$ values for this and the base model produces an almost linear trend with a slope of 0.2 (Fig. 10b).

*Viscosity contrast*—in this model the viscosity of boudins was taken as $\eta = 3e20$, so that the viscosity ratio of boudin to matrix is $M = 30$. Some tests were also done for $M = 90$. Viscosity contrast does not affect the vergence sense of developed asymmetries but, since boudins behave in a more competent way, the component of rigid-body rotation increases (Fig. 9). Thus, an increase in viscosity

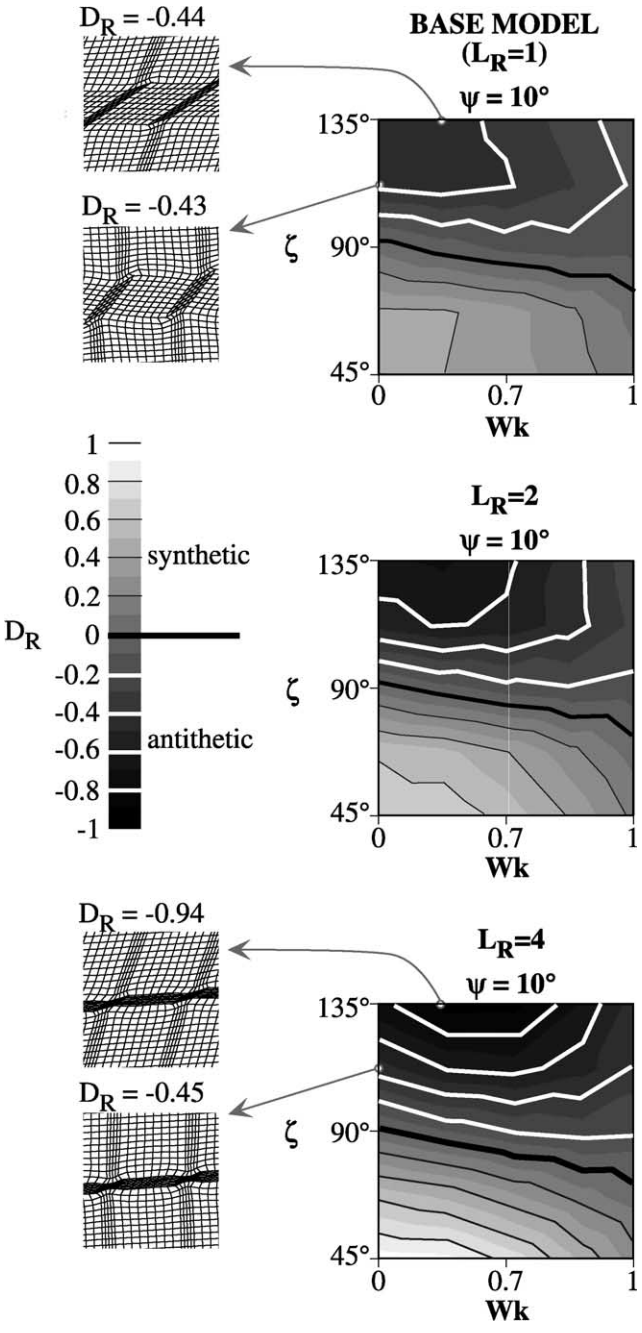


Fig. 11. $D_R$ contours plotted in diagrams of $W_k$ versus $\zeta$ at $\psi = 10°$ for the base model, a model with $L_R = 2$ and a model with $L_R = 4$, respectively, all deformed to $R = 2$. Solid black contour lines represent lines of zero offset separating synthetic slip and antithetic slip boudinage. The position of the $D_R = 0$ curve remains almost constant for the three models but offset increases with aspect ratio at low and high $\zeta$ values. This is shown by the examples of deformed grids.

contrast has the opposite effect to an increase in $L_R$. Rotation of boudins increases with viscosity contrast, whereas boudin separation or extension across boudins shows little modification. Viscosity ratio also has an influence on the modification of boudin shape, barrel-shaped irregularities being less developed as boudin viscosity increases. Similar effects were found in numerical models by Treagus and Lan (2000) who observed the greatest barrelling effect for $M = 5$ and showed that for $M$ values greater than 20 objects behave more nearly rigid.

$D_R$ clearly increases with viscosity ratio (Figs. 9, 10b and 12). Comparison of $D_R$ values for $M = 10$ and 30 produces an almost linear trend with a slope of 1.4 (Fig. 10b).

*Power law boudins*—the effect of non-linear elasto-viscous behaviour of boudins was also tested. In these models the boudin train follows a power law relationship $d\epsilon/dt = A\sigma^n$, where $A$ is the pre-exponential constant (taken as $2.3e-34\ Pa^{-n}\ s^{-1}$) and $n$ the stress exponent (taken as three). The value for the pre-exponential material constant $A$ was chosen to maintain a similar effective viscosity to that of boudins in the base models. The incompetent matrix is of linear elasto-viscous rheology. The results on boudin rotation and offset are very similar to those obtained for the models with a viscosity contrast $M = 30$, as shown by the similar styles of asymmetric boudinage in Fig. 9 and similar slopes in Fig. 10b. However, a slightly greater modification in shape occurs; power law boudins have more sigmoidal corners than boudins in the base model, whereas boudins with $M = 30$ show almost no heterogeneity in shape.

The experiments presented above that deviate from the base-model indicate that rheological and geometrical parameters other than $\psi$ and $\zeta$ influence the magnitude of displacement and boudin rotation to some extent, but that they do not significantly influence the $D_R$-vergence. $D_R$ increases with increasing viscosity ratio and also increases with aspect ratio (shape factor $L_R$; Fig. 11). On the other hand, $D_R$ decreases in the models 'gap fill' and 'connected boudins' relative to the base model. This implies that the simple base model can be used as an analogue for boudins of different shape and rheology for movement sense analysis, but not for quantitative analyses.

## 7. Discussion

### 7.1. Significance for natural boudins

The FLAC modelling presented above shows that for monoclinic initial geometry of a boudinaging layer and of the bulk flow, development of asymetric boudins is most strongly influenced by $\psi$, $\zeta$ and $W_k$ and less by other factors such as boudin length, nature of the interboudin zone or boudin rheology. The response for a certain initial geometry of $\psi$ and $\zeta$ for the range of possible $W_k$ values is summarised in Fig. 6a and b and shows a tendency of antithetic slip boudins to develop preferentially at high $\zeta$ values. At high $W_k$ approaching simple shear, antithetic slip boudins are likely to develop over a larger range of $\zeta$, including rectangular ones, down to low $\zeta$ values. Synthetic slip boudins are likely to develop at low $\zeta$ as in shear band geometry, and are favoured at lower $W_k$ such as in transpression. The effect of increasing $\psi$ is mainly to increase the field of synthetic slip boudinage to higher $\zeta$ values so that not only boudins

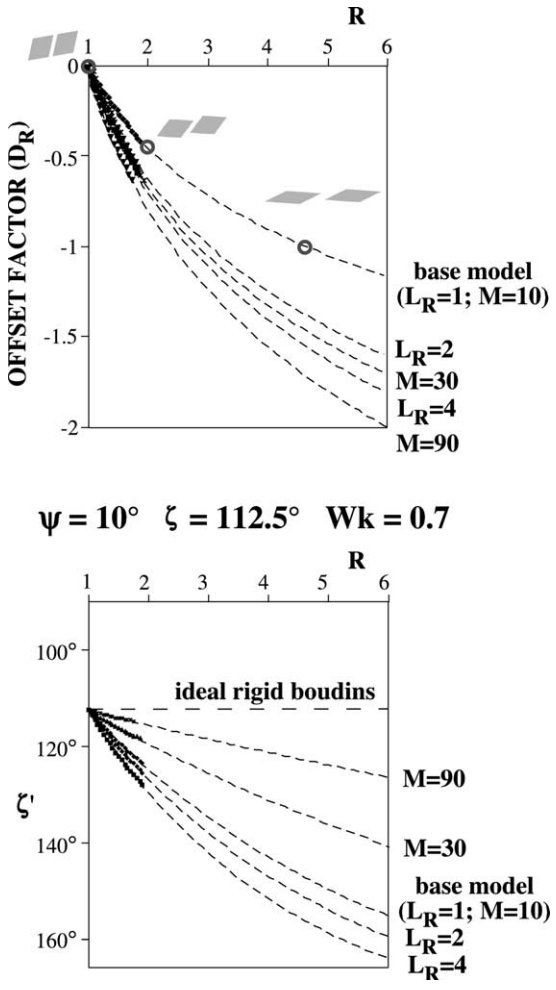


Fig. 12. Graphs showing how $D_R$ and $\zeta'$ are likely to develop with increasing strain ratio $R$ for a particular geometry and for $\psi = 10°$, $\zeta = 112.5°$ and $W_k = 0.7$. These values are applied to the base model, to two models with higher viscosity ratio ($M = 30$ and $M = 90$) and to two models with higher aspect ratio ($L_R = 2$ and 4). Values from numerical modelling were extrapolated forward to predict the response at high strain.

with a shear band geometry due to low $\zeta$, but also rectangular boudins tend to show synthetic slip (Fig. 6b). It is therefore mainly the mechanism of boudin initiation, creating the interboudin zones and setting $\zeta$ that determines which kind of asymmetric boudins will develop.

Several authors have described the geometry and shear sense of natural asymmetric boudins (Hanmer, 1986; Gaudemer and Taponnier, 1987; Malavieille, 1987; Marcoux et al., 1987; Goldstein, 1988; Malavieille and Lacassin, 1988; Hanmer and Passchier, 1991; Goscombe and Passchier, 2002). None of these authors were able to determine $W_k$ or other flow conditions from field observations, but most $\psi$ values in their studies seem to be close to 0°. Their results generally agree with the outcome of our tests: highly asymmetric boudin blocks, with initially low $\zeta$, are usually developed as synthetic slip boudins. Those with square shapes and initially high $\zeta$ are developed as antithetic slip boudins. This would imply that most of these boudins formed in high strain zones where $W_k$ must have been high. $\zeta'$ values exceeding 90° are commonly associated with FF-deflection and strong internal deformation of the boudins, and may therefore develop from initially rectangular boudins, while boudins with $\zeta'$ values below 90° rarely show FF-deflection but commonly FS-deflection. $\zeta'$ may be close to original $\zeta$ values in this case.

### 7.2. Practical application

In order to use boudins as shear sense indicators or even as tools for a more complex kinematic analysis, it is necessary to find geometric characteristics of boudin groups with antithetic or synthetic slip on the interboudin zone, respectively. Only thus is it possible to establish whether the geometry in Fig. 2b formed in dextral or sinistral non-coaxial flow. $\zeta'$ can be measured in the field, and $\psi'$ can be determined if we assume that the extensional eigenvector of flow coincides with the shear zone boundary, or that it is close to a well-developed foliation. It is questionable, however, if knowledge of $\zeta'$ and $\psi'$ are sufficient to determine shear sense. There are two important restrictions:

1. Our model is based on initial angles $\zeta$ and $\psi$. The amount of change of the initial $\zeta$ and $\psi$ to $\zeta'$ and $\psi'$ depends on a number of parameters in a complex manner. For a layer undergoing extension, the absolute value of $\psi'$ decreases as for a material line. $\zeta$ only changes if the effective viscosity contrast between boudins and matrix is relatively small and in that case, $\zeta'$ normally increases with progressive deformation. The change in $D_R$ and $\zeta'$ with finite strain for different deformation parameters is given in Fig. 12 for models of different aspect and viscosity ratios but the same $W_k$ and initial $\zeta$ and $\psi$. Only changes at small finite strain could be measured and these are extrapolated to higher strain based on the base model curve. Unless finite strain and effective viscosity ratio between boudins and matrix are known, it is therefore not possible to construct diagrams like Fig. 6a in order to find the position of a $D_R = 0$ curve for $\zeta'$ and $\psi'$ instead of $\zeta$ and $\psi$.
2. Every graph in Fig. 6a has a mirror image equivalent for bulk sinistral shear. Distinction between such mirror image graphs is only possible if the shear sense or initial 'sense' of $\zeta$ (larger or smaller than 90°) is known, and this hampers the use of asymmetric boudins as primary, independent shear sense markers. The same applies to $\psi'$: it may be difficult to decide if $\psi'$ is positive or negative in the field. Instead of $\zeta$ or $\zeta'$ we therefore have to use an angle $\theta$, which ranges only between 0 and 90° and where

$$\theta = \zeta' \text{ if } 0° < \zeta' < 90° \text{ and } \theta = 180° - \zeta' \text{ if } 90° < \zeta' < 180° \quad (3)$$

Fig. 13 shows graphs similar to those of Fig. 6, collapsed from $\zeta$ to $\theta$ values. For most $W_k - \theta$ values in Fig. 13a,

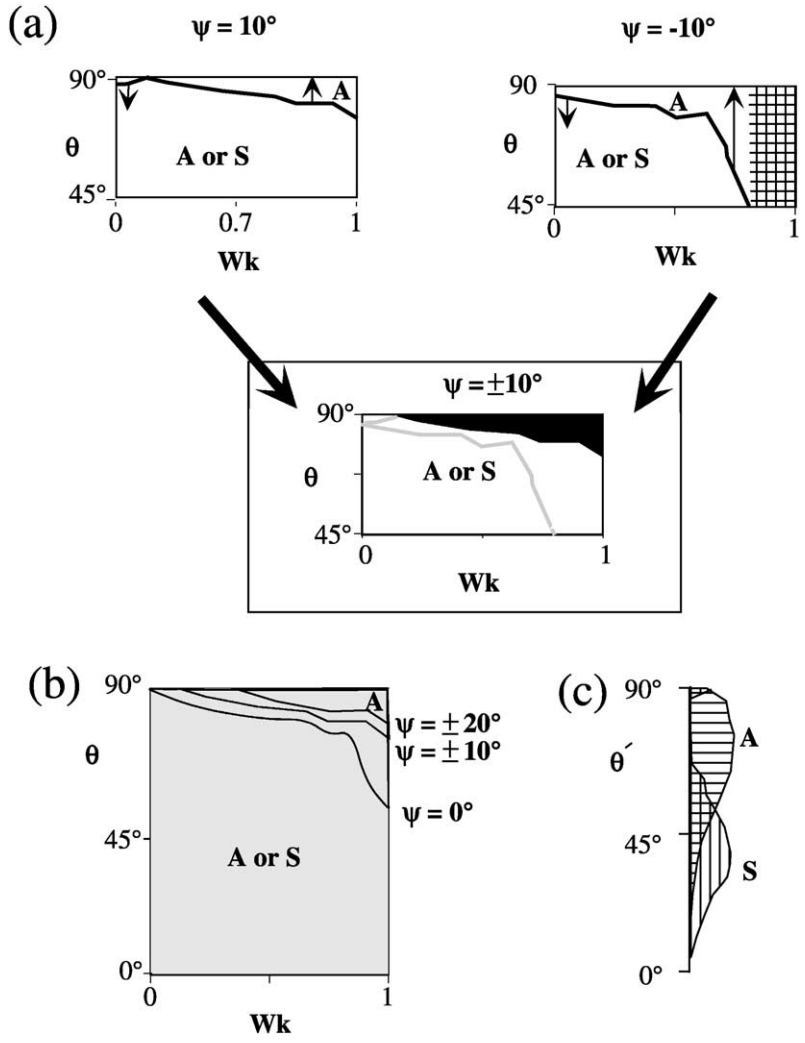


Fig. 13. (a) Distribution of antithetic slip ($A$) and synthetic slip ($S$) boudins in $\theta - W_k$ diagrams for $\psi = 10$ and $-10°$ derived from Fig. 6a. Arrows indicate the development of $\theta'$ with increasing strain if boudins deform internally. Both diagrams can be combined if the positive or negative nature of $\psi$ is unclear: in the resulting $\theta - W_k$ diagram (box), the small black domain, the antithetic window, is of exclusive antithetic-slip boudins. Outside this window, the antithetic or synthetic nature of interboudin slip cannot be separated. (b) $\theta - W_k$ diagram showing the effect of $\psi$ on the size of the antithetic window. The graph at right is the collapsed equivalent of Fig. 6c.

interboudin slip can be synthetic or antithetic but there is a small wedge-shaped zone at high $W_k$ and $\theta$ close to 90° where slip is always antithetic, the 'antithetic window'. This wedge-shaped zone changes shape if $\theta$ is deformed to less-orthogonal angles (arrows). This implies that only approximately rectangular asymmetric boudins at high $W_k$, which plot in the antithetic window will be reliable shear sense indicators in all cases, based on just the angle $\theta$. At lower $\theta$ and $W_k$ values it is more difficult to determine shear sense. However, for the most common category of boudins with $\psi'$ close to zero the following will apply.

Synthetic slip boudins with low $\zeta'$ may have undergone little modification from the original $\zeta$, since the angular velocity of a material line such as an interboudin plane at low $\zeta$ is smaller than for rectangular boudins. Also, since such boudins will show little separation (Fig. 7), they may develop FS-deflection. Rectangular boudins, with $\zeta$ close to 90° develop into antithetic slip boudins with high separation (Fig. 7). If they deform internally, they will develop into high $\zeta'$ boudins ($\zeta' > 90°$) with evidence for internal deformation, and possibly with FF-deflection. Originally high $\zeta$ boudins (exceeding 90°) are probably rare since they do not represent a favourable nucleation orientation for brittle or ductile extensional or shear zones. If formed, they will not show much rotation of the interboudin plane to still higher $\zeta'$ values but high separation, and therefore little or no FS-deflection. Therefore, boudins with $\zeta' > 90°$ are in the same low $\theta'$ range as boudins with $\zeta' < 90°$ in opposite shear sense, but they may be distinguished as follows. Low $\theta'$ boudins with little internal deformation, FS-deflection and little separation are likely to be synthetic slip boudins ($\zeta' < 90°$); low $\theta'$ boudins with strong internal deformation, FF-deflection and high separation are likely to be antithetic slip boudins ($\zeta' > 90°$).

Goscombe and Passchier (2002) investigated natural asymmetric boudins in outcrops with known shear sense and found that $\theta'$ in combination with deflection sense on the interboudin plane (FF- or FS-deflection) and boudin length–width ratio allow separation of boudin groups with antithetic and synthetic slip in the field in most cases. They found that there is no complete overlap in $\theta'$ between antithetic and synthetic slip groups in natural asymmetric boudins, even if $\zeta'$ (Fig. 6c) is collapsed to $\theta'$ (Fig. 13c).

The interpretation of low $\theta$ boudins can also be improved if the positive or negative sense of $\psi'$ is known. A layer is extending in monoclinic flow if $\psi$ is positive or if it is negative and

$$|\psi| < 0.5\arccos(W_k) \quad (4)$$

Large negative values of $\psi$ or $\psi'$ therefore imply shortening rather than extension and boudinage of a layer. If, therefore, the absolute value of $\psi'$ is large *and* the layer is boudinaged and was therefore extending, then $\psi'$ must be positive. This implies that the curves for positive $\psi$ in Fig. 6 can be used to assess the significance of $\theta$. $\psi$ can even act as a separate shear sense indicator as follows. If $\psi$ is positive and inclined to the left with respect to the shear zone boundary (e.g. Fig. 5), shear sense is dextral, and vice versa. Finally, although it largely depends on the viscosity contrast and on strain intensity, barrelling of boudins and boudin separation can to some extent be used as a kinematic indicator. At low $\theta'$ values, barrelling of boudins indicates low $W_k$. Large boudin separation generally also indicates low $W_k$.

## 8. Conclusions

Asymmetric boudins are complex shear sense indicators. Sense of slip (synthetic, antithetic) with respect to shear sense of flow in the host rock for boudins with a monoclinic symmetry is determined by the angle of the interboudin zone with the boudin surface, the kinematic vorticity number, and the orientation of the boudin train with respect to the extensional flow eigenvector. Other geometric and rheological factors (i.e. length/width ratio and viscosity ratio) influence the magnitude of offset along the neck regions but not the sense of slip. The numerical analysis presented here mostly agrees with previous experimental and analytical models. We find that the bulk sense of shear in natural shear zones can be determined from the orientation of the interboudin zone of asymmetric boudinage structures in rare cases, but in most general situations additional data on boudin geometry and orientation are needed. Excessively simplistic models and assumptions (e.g. simple shear flow) should be avoided since they may lead to erroneous interpretations.

## Acknowledgements

This work was partly carried out at the University of Melbourne during a sabbatical leave of CP. CP thanks the University of Melbourne for financial support. Chris Wilson, Roger Powell and Brett Marmo are thanked for their help. ED thanks the European Commission and the University of Mainz for a post-doctoral research grant (Marie Curie–TMR) at the University of Mainz. We also thank Paul Bons and Jordi Carreras for their profitable suggestions, and Y. Zhang and ITASCA-personnel for useful advice on computer simulation with FLAC. Constructive reviews by Neil Mancktelow and Geoffrey Lloyd are gratefully acknowledged.

## References

Cloos, E., 1947. Boudinage. Transaction of the American Geophysical Union 28, 626–632.

Cundall, P., 1991. Shear band initiation and evolution in frictional materials ASCE Eng. Mech. Speciality Conf., Columbus, OH, USA, Session 2.

Druguet, E., Passchier, C.W., Carreras, J., Victor, P., den Brok, S., 1997. Analysis of a complex high-strain zone at Cap de Creus, Spain. Tectonophysics 280, 31–44.

Etchecopar, A., 1977. A plane kinematic model of progressive deformation in a polycrystalline aggregate. Tectonophysics 39, 121–139.

Gaudemer, Y., Taponnier, P., 1987. Ductile and brittel defomations in the northern Snake Range, Nevada. Journal of Structural Geology 9, 159–180.

Ghosh, S.K., Ramberg, H., 1976. Reorientation of inclusions by combination of pure and simple shear. Tectonophysics 34, 1–70.

Goldstein, A.G., 1988. Factors affecting the kinematic interpretation of asymmetric boudinage in shear zones. Journal of Structural Geology 10, 707–715.

Goscombe, B.D., Passchier, C.W., 2002. Asymmetric boudins as shear sense indicators—an assessment from field data. Journal of Structural Geology, in review.

Grasemann, B., Stüwe, K., 2001. The development of flanking folds during simple shear and their use as kinematic indicators. Journal of Structural Geology 23, 715–724.

Gutierrez, M., Cuisiat, F., 1999. Predicting sub-seismic faulting from strain localisation. In: Detournay, A., Hart, G. (Eds.). FLAC and Numerical Modeling in Geomechanics. Balkema, Rotterdam, pp. 173–181.

Hanmer, S., 1986. Asymmetric pull-aparts and foliation fish as kinematic indicators. Journal of Structural Geology 8, 111–122.

Hanmer, S., Passchier, C.W., 1991. Sense of shear markers in rocks. Geological Survey of Canada Paper 90-17.

Hobbs, B., Ord, A., 1989. Numerical simulations of shear band formation in a frictional-dilatant material. Ingenieur-Archiv 59, 209–220.

Hudleston, P.J., 1989. The association of folds and veins in shear zones. Journal of Structural Geology 11, 949–957.

Itasca Consulting Group, Inc., 1998. FLAC: Fast Lagrangian Analysis of Continua, Version 3.40. Itasca Consulting Group, Inc., Minneapolis.

Jiang, D., Williams, P.F., 1998. High-strain zones: a unified model. Journal of Structural Geology 20, 1105–1120.

Jordan, P.G., 1991. Development of asymmetric shale pull-aparts in evaporite shear zones. Journal of Structural Geology 13, 399–409.

Kidan, T.W., Cosgrove, J.W., 1996. The deformation of multilayers by layer normal compression; an experimental investigation. Journal of Structural Geology 18, 461–474.

Lloyd, G.E., Ferguson, C.C., 1981. Boudinage structure: some interpretations based on elastic–plastic finite element simulations. Journal of Structural Geology 3, 117–128.

Lohest, M., 1909. L'origine des veines et des géodes des terrains primaires de Belgique. Annales de la Société géologique Belgique 36B, 275–282.

Malavieille, J., 1987. Kinematics of compressional and extensional ductile

shearing deformation in a metamorphic core complex of the northeastern Basin and Range. Journal of Structural Geology 9, 541–554.

Malavieille, J., Lacassin, R., 1988. 'Bone-shaped' boudins in progressive shearing. Journal of Structural Geology 10, 335–345.

Mancktelow, N.S., 1999. Finite-element modelling of single-layer folding in elasto-viscous materials: the effect of the initial perturbation geometry. Journal of Structural Geology 21, 161–177.

Mandal, N., Khan, D., 1991. Rotation, offset and separation of oblique-fracture (rhombic) boudins: theory and experiments under layer-normal compression. Journal of Structural Geology 13, 349–356.

Mandal, N., Chakraborty, C., Samanta, S.K., 2000. Boudinage in multilayered rocks under layer-normal compression: a theoretical analysis. Journal of Structural Geology 22, 373–382.

Marcoux, J., Brun, J.-P., Ricou, L.E., 1987. Shear structures in anhydrite at the base of thrust sheets (Antalya, southern Turkey). Journal of Structural Geology 9, 555–561.

Marmo, B.A., Wilson, C.J.L., 1999. A verification procedure for the use of FLAC to study glacial dynamics and the implementation of an anisotropic flow law. In: Detournay, A., Hart, G. (Eds.). FLAC and Numerical Modeling in Geomechanics. Balkema, Rotterdam, pp. 183–190.

McKinnon, S.D., Garrido de la Barra, I., 1998. Fracture initiation, growth and effect on stress field: a numerical investigation. Journal of Structural Geology 20, 1673–1689.

Means, W.D., Hobbs, B.E., Lister, G.S., Williams, P.F., 1980. Vorticity and non-coaxiality in progressive deformation. Journal of Structural Geology 2, 371–378.

O'Driscoll, E.S., 1964. Rheid and rigid rotations. Nature 203, 832–835.

Ord, A., 1990. Mechanical controls on dilatant shear zones. In: Knipe, R.J., Rutter, E.H. (Eds.), Deformation Mechanisms, Rheology and Tectonics. Geological Society London Special Publication 54, pp. 183–192.

Passchier, C.W., 1998. Monoclinic model shear zones. Journal of Structural Geology 20, 1121–1137.

Passchier, C.W., 2001. Flanking structures. Journal of Structural Geology 23, 951–962.

Poliakov, A.N.B., Herrmann, H.J., 1994. Self-organized criticality in plastic shear bands. Geophysical Research Letters 21, 2143–2146.

Poliakov, A.N.B., Podladchikov, Y., Dawson, E.Ch., Talbot, C.J., 1996. Salt diapirism with simultaneous brittle faulting and viscous flow. In: Alsop, I., Blundell, D., Davison, I. (Eds.), Salt Tectonics. Geological Society London Special Publication 100, pp. 291–302.

Ramberg, H., 1955. Natural and experimental boudinage and pinch-and-swell structures. Journal of Geology 63, 512–526.

Ramsay, A.C., 1881. The geology of North Wales. Memoirs of the Geological Survey of Great Britain 3.

Ramsay, J.G., 1967. Folding and Fracturing of Rocks. McGraw-Hill, New York.

Selkman, S., 1978. Stress and displacement analysis of boudinage by the finite-element method. Tectonophysics 44, 115–139.

Stephanson, O., Berner, H., 1971. The finite-element method in tectonic processes. Physics of the Earth and Planetary Interiors 4, 301–321.

Strömgard, K.E., 1973. Stress distribution during formation of boudinage and pressure shadows. Tectonophysics 16, 215–248.

Swanson, M.T., 1992. Late Acadian–Alleghenian transpressional deformation: evidence from asymmetric boudinage in the Casco Bay area, coastal Maine. Journal of Structural Geology 14, 323–341.

Treagus, S.H., Lan, L., 2000. Pure shear deformation of square objects, and applications to geological strain analysis. Journal of Structural Geology 22, 105–122.

Turcotte, D.L., Schubert, G., 1982. Geodynamics: Applications of Continuum Physics to Geological Problems. Wiley, New York.

Wilson, C.J.L., Zhang, Y., 1994. Comparison between experimental and computer modelling of plane-strain simple shear ice deformation. Journal of Glaciology 134, 46–55.

Zhang, Y., Hobbs, B.E., Jessell, M.V., 1994. The effect of grain boundary sliding on fabric development in polycrystalline aggregates. Journal of Structural Geology 16, 1315–1325.

Zhang, Y., Hobbs, B.E., Ord, A., Mühlhaus, H.B., 1996. Computer simulation of single-layer buckling. Journal of Structural Geology 18, 643–655.